RESEARCH ARTICLE

Global measurement of water waves by Fourier transform profilometry

**Pablo Javier Cobelli · Agnès Maurel ·
Vincent Pagneux · Philippe Petitjeans**

Abstract In this paper, we present an optical profilo-
metric technique that allows for single-shot global
measurement of free-surface deformations. This system
consists of a high-resolution system composed of a vid-
eoprojector and a digital camera. A fringe pattern of known
characteristics is projected onto the free surface and its
image is registered by the camera. The deformed fringe
pattern arising from the surface deformations is later
compared to the undeformed (reference) one, leading to a
phase map from which the free surface can be recon-
structed. Particularly, we are able to project wavelength-
controlled sinusoidal fringe patterns, which considerably
increase the overall performance of the technique and the
quality of the reconstruction compared to that obtained
with a Ronchi grating. In comparison to other profilometric
techniques, it allows for single-shot non-intrusive mea-
surement of surface deformations over large areas. In
particular, our measurement system and analysis technique
is able to measure free surface deformations with sharp
slopes up to 10 with a 0.2 mm vertical resolution over an
interrogation window of size 450×300 mm^2 sampled
on approximately 6.1×10^6 measurement points. Some
illustrative examples of the application of this measuring
system to fluid dynamics problems are presented.

P. J. Cobelli (✉) · P. Petitjeans
Laboratoire de Physique et Mécanique des Milieux Hétérogènes,
UMR CNRS 7636, École Supérieure de Physique et de Chimie
Industrielles, 10 rue Vauquelin, 75231 Paris Cedex 05, France
e-mail: cobelli@pmmh.espci.fr

A. Maurel
Laboratoire Ondes et Acoustique, UMR CNRS 7587, École
Supérieure de Physique et de Chimie Industrielles,
10 rue Vauquelin, 75231 Paris Cedex 05, France

V. Pagneux
Laboratoire d'Acoustique de l'Université du Maine,
UMR CNRS 6613, Avenue Olivier Messiaen,
72085 Le Mans Cedex 9, France

1 Introduction

Free-surface water waves phenomena enjoys an unceasing
interest from both the fluid scientists and engineering
communities. In general, the defining characteristic of free-
surface flows is the presence of a deformable interface,
which by itself provides for an interaction mechanism
between the base flow and the external environment. For a
vast variety of cases, this interaction is far from being
negligible, and often its effects can lead to a drastic change
in the hydrodynamical characteristics and time evolution of
the flow. In such flows, the interaction between the inter-
face and the underlying flow is made evident in the form of
deformations of the free surface. The detailed shape of
these deformations is determined by a delicate balance
between the local pressure below the surface and its ver-
tical acceleration, on one hand, and gravity and interfacial
tension (associated with the surface's local curvature), on
the other.

Therefore, the experimental study of free-surface defor-
mation (herein referred to as FSD) in free-surface flows
constitutes the keystone to understanding the complex
mechanisms that govern its interaction with the underlying
near-surface flow. In recent years, many theoretical,
numerical and experimental studies on free surface defor-
mation were conducted to understand its interaction with a
vast variety of basic flows, such as vortices and vortex rings
(Ruban 2000; Gharib 1994; Gharib and Weigand 1996), as
well as jets (see, e.g., Walker et al. 2006), as well as with

turbulent flows (Savelsberg et al. 2006; Savelsberg and van de Water 2008).

Although much work has been done to aid our understanding of FSD, it is clear that both theoretical predictions and numerical results still need detailed experimental validation through a suitable measuring technique.

Standard measuring techniques for FSD in fluid flows are usually to a few point measurements, employing either one or an array of gauges. These methods only allow for discrete localized measurements, so that the information on the 2D aspects of FSD and disturbances' propagation is incomplete. These limitations and deficiencies led fluid experimentalists to the development of novel optical techniques for the accurate measurement and tracking of the 3D-topography of FSDs.

Cox (1958) determined the surface elevation by the refraction of light through the free-surface. A light source of spatially linearly-varying intensity was placed at the bottom of a water tunnel and a telescope imaged one point on the water surface into a photocell. The intensity of the light recorded by the photocell is related to one component of the slope of the free-surface. This technique is commonly known as "refractive mode" since the light rays are refracted through the surface. Likewise, a technique known as "reflective mode" permits observation of the free surface by illumination of the liquid surface from above. Zhang and Cox (1994) and Zhang et al. (1994) devised a technique for measuring the FSD by using a free-surface gradient detector (FSGD). The principle behind this method is to color-code the surface slopes (for further details on the technique, see Zhang et al. 1996; Zhang 1996). This technique was later combined with digital particle image velocimetry (Dabiri and Gharib 2001; Dabiri 2003) to study near-surface flows by constructing correlations between small-sloped FSDs and near-surface velocities.

Diffusing light photography was employed by Wright et al. (1996) to study FSD under fully developed isotropic ripple turbulence, and later on for the imaging of intermittency (Wright et al. 1997). In their technique, the fluid is illuminated from below with a 10-μm light flash that diffuses through the liquid as a result of multiple scattering from a diluted suspension of 1-μm-polystyrene spheres. Light intensity reaching the air–liquid interface depends on the local depth, so that less light penetrates deeper regions. Calibrating the transmission of light as a function of fluid depth leads to the instantaneous height of the fluid surface, even when it presents large variations in height and curvature. This technique works for light transport mean free paths (i.e., the distance over which a ray scatters through a large angle) larger than the surface displacement but smaller than the fluid depth. Although precise, this technique is very delicate to implement

particularly due to the constraints imposed on particle concentration control. For measuring the global FSD caused by the interaction of surface waves impinging on a single fixed vortex, Vivanco and Melo (2004) scanned the whole surface measuring at each point the deflection of a reflected laser beam. Although the method provides for a measure of the amplitude and phase of the surface deflection, its range of application is limited to stationary or periodic processes. Tsubaki and Fujita (2005) and Benetazzo (2006) presented two different stereoscopic methods for measuring 2D water surface configurations. Their method consists on using a pair of sequential images captured by two cameras arranged in stereo position. This method is suitable for the accurate measurement of both small-amplitude waves and surface discontinuities. Recently, Moisy et al. (2008) proposed an optical technique based on digital image correlation. A set of random points printed at the bottom of a channel is observed through the deformed surface. The apparent displacement field observed between the refracted and the reference images allows for the determination of the local surface slope. Being a refractive technique, the main limitation of the method is due to caustics generated by strong curvature or large surface-pattern distance.

Fringe projection profilometry was first employed by Grant et al. (1990) to measure the FSD associated to water waves using the projection moiré method (see e.g. Patorski 1993). However, wave probes had to be used to resolve the ambiguity associated to the polarity of the fringes (i.e., which fringes represent peaks and which represent throughs) and to obtain an absolute measure of elevation above the mean water level. Zhang and Su (2002) proposed a particular fringe projection profilometric technique commonly known as Fourier transform profilometry (FTP) (see Takeda et al. 1982; Takeda and Mutoh 1983; Su and Chen 2001) for the measurement of FSDs and presented experimental results on a vortex' shape at a free surface. Recently, Cochard and Ancey (2008) developed a measuring system based on Phase Shifting and FTP applied to the dam-break problem (i.e., the sudden release of a volume of liquid down a slope) and measured the time-evolution of the flow.

In order to further our understanding of FSD mechanisms, this paper presents an optical profilometry technique that allows for high-resolution 3D whole-field reconstruction of time-dependent FSD fields. Our technique is based on fringe projection profilometry, which has been successfully employed for the topography of solid surfaces in a wide variety of fields, such as 3D sensing systems, mechanical engineering, machine vision, robotic control, industry monitoring and quality assesment, biomedicine, etc. In this work, we propose both the liquid surface extension of this technique along with several significant

improvements in the optical setup as well as in the signal processing algorithm.

Our presentation is organized in five sections as follows. Section 2 briefly summarizes the principle of FTP, upon which our measuring technique is based. In Sect. 3, we describe both the complete experimental system, measurement protocol and data processing algorithm developed to measure the liquid's free-surface deformation. Limitations of the method, such as maximum range of measurement, system's resolution and accuracy are discussed as well. Section 4 is divided into three sections providing diverse illustrative applications of our measuring technique. Finally, the last section presents concluding remarks.

2 Principle of the method

Although there exists a vast variety of implementations of fringe projection profilometry, the underlying principle common to all of them is very simple. In its more elementary form, a typical fringe projection profilometry setup consists of a projection device and an image recording system. A fringe pattern of known characteristics is projected onto the test object and the resulting image is observed from a different direction. Since projection and observation directions are different, the registered fringe pattern is distorted according to the object's profile and perspective. From the point of view of information theory, we could say that the object's depth information is encoded into a deformed fringe pattern recorded by the acquisition sensor, allowing it to be measured by comparison to the original (undeformed) grating image. It is therefore the phase shift between the reference and deformed images which contains all the information of the deformed object.

In this paper, we present an improvement of both the measuring system and the analysis algorithm based on a particular fringe projection profilometry known as FTP, first introduced by Takeda et al. (1982).

In its simplest formulation, and without entering into the details of the associated experimental setups (which we will address in Sect. 3), the principle of the method can be explained as follows, where we distinguish the optical principle from the signal processing algorithm.

2.1 Optical principle

Figure 1 shows the optical setup: the camera and the projector are chosen to be arranged in the parallel–optical-axes geometry, i.e., their optical axis are parallel to each other and separated by a length D. They are perpendicular to the reference plane (Oy), which corresponds to the undeformed
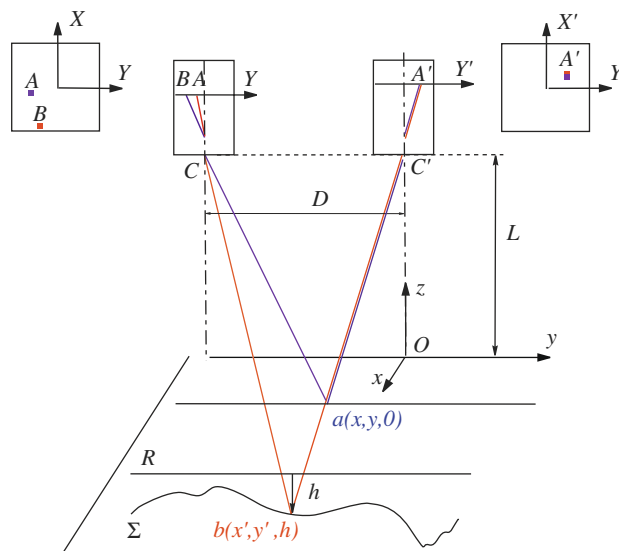

Fig. 1 Optical configuration scheme and ray tracing for the projection and imaging system. Parallel–optical-axes geometry is adopted: both optical axes are coplanar and parallel to each other, separated by a distance D, while the entrance pupils are positioned at the same height, L over the undeformed reference surface. [The point of coordinates (x', y', h) in the figure corresponds to $(x + \delta x, y + \delta y, h)$ in the notation used for the text]

surface. In addition, their entrance pupils are located at the same height L[1].

We start from the simple configuration where (Oy) is a reflecting surface. From a periodic pattern with p_p-period on (Y), the projector forms[2] a p-periodic pattern on (Oy), with a magnification $\alpha (p = \alpha p_p, \alpha > 1)$. Then, the pattern on (Oy) is seen by the camera that restitutes a p_c-periodic pattern on (Y'), with a magnification $\beta (p_c = \beta p, \beta < 1)$. This two-step process can be described using rays: the ray coming from A on (Y) [with some intensity level, or "phase" $\varphi(A)$] goes to a on (Oy), afterwards it enters the camera reaching (Y') at a point A'. Since the intensity level is conserved along the ray path, the phase at A on the projector, the phase on the undeformed surface at a, and the phase at A' on the camera are equal, i.e., $\varphi_0(A) = \varphi_0(a) = \varphi_0(A')$. The phase on the camera is called φ_0 when the reflecting surface is undeformed (Oy) and φ when the reflective surface is deformed (S). In the latter case, although the reflecting surface does not coincide with (Oy), the same analysis holds but $\varphi(A') \neq \varphi_0(A')$. Indeed, A' is now the image formed by the ray that enters the camera coming from b: $\varphi(A') = \varphi(b)$. The phase at b is the same as the phase of point B on (Y) that differs from A, thus $\varphi(A') = \varphi(b) = \varphi(B)$.

---

[1] As a matter of fact, these conditions are not necessary but strongly simplify the equations. Moreover, Chan et al. (1994) have showned that the parallel–optical-axes geometry provides a wider range of measurement.

[2] In the case of a transparent liquid, projection onto its free surface is attained by the addition of dye. See Sect. 3.1. for further details.

Measuring the deformed surface implies not only to calculate the height $h(b)$, as usually only done, but also calculating the corresponding position $(x + \delta x, y + \delta y)$ where it is indeed measured (Fig. 1).

Elementary geometrical optics can be used to get (see Takeda and Mutoh 1983; Rajoub et al. 2007; Maurel et al. 2009)

$$h = \frac{\Delta\varphi L}{\Delta\varphi - 2\pi/p\, D}, \tag{1}$$

$$\delta y = \frac{D - y}{L} h, \tag{2}$$

$$\delta x = \frac{x}{L} h, \tag{3}$$

where $\Delta\varphi(Y) \equiv \varphi(Y) - \varphi_0(Y)$. Then the measurement of the height distribution h and the corresponding positions $(x + \delta x, y + \delta y)$ of the deformed surface consists of determining this phase-shift.

Intermediate, but useful relations are the intensities (gray scales) recorded by the camera I_0 and I when the reflecting surfaces are, respectively, (Oy) and (S) and for a sinusoidal fringe pattern (see also Sects. 3.1, 3.4).

$$I_0(X, Y) = \cos(2\pi/p_c Y + \varphi_0(Y)), \quad \varphi_0 = -\frac{2\pi}{p}D$$

$$I(X, Y) = \cos(2\pi/p_c Y + \varphi(Y)), \quad \varphi = -\frac{2\pi}{p}\frac{D}{L - h}, \tag{4}$$

These four last relations are the ones proposed by Takeda et al. (1982) using $f_0 \equiv 2\pi/p$.

2.2 Signal processing

The camera records the intensity signals $I(X, Y)$ and $I_0(X, Y)$. These signals differ from the simplified form given by Eq. 5 mainly because of two sources of unwanted intensity variations. The first consists of illumination inhomogeneities or background variations over the field of view $\mathcal{B}$, and is made evident when no grating pattern is used. In that case, the intensity registered by the camera can therefore be expressed as

$$I^{\text{ref}}(X, Y) = \mathcal{B}(X, Y). \tag{5}$$

These inhomogeneities remain present when the fringe pattern is projected, as well as when the reflecting surface is deformed, as an additive variation. The second source of unwanted intensity variation is typically due to a modulation on the intensity of the projected pattern of fringes. This modulation, corresponding to a local surface reflectively, is denoted $\mathcal{A}$, and remains the same (or almost the same) whatever being the height of the reflecting surface. These result in the general form of the recorded intensities as

$$I_0(X, Y) = \mathcal{A}(X, Y)\cos(2\pi/p_c Y + \varphi_0(Y)) + \mathcal{B}(X, Y),$$

$$I(X, Y) = \mathcal{A}(X, Y)\cos(2\pi/p_c Y + \varphi(Y)) + \mathcal{B}(X, Y),$$
$$\tag{6}$$

Basically, the signal treatment can be divided in two steps.

Step 1 mainly consists in the suppression of the additive background in both the reference and deformed image, and is given by the following equations:

$$\mathcal{H}(I_0 - I^{\text{ref}}) = \mathcal{A}(X, Y)\exp\{i(2\pi/p_c Y + \varphi_0(Y))\}, \tag{7}$$

$$\mathcal{H}(I - I^{\text{ref}}) = \mathcal{A}(X, Y)\exp\{i(2\pi/p_c Y + \varphi(Y))\}, \tag{8}$$

where $\mathcal{H}(F)$ denotes the Hilbert transform of F and i stands for the imaginary unit. It has been assumed that the typical length of variation in $\mathcal{A}$ is large compared to the wavelength p of the projected pattern (in our case, $p = 2$ mm against typical 10 cm variation length for $\mathcal{A}$).

Step 2 allows us to recover the phase shift $\Delta\varphi$ between the two images just by taking the imaginary part of

$$\log\left[\mathcal{H}(I - I^{\text{ref}}) \cdot \mathcal{H}^*(I_0 - I^{\text{ref}})\right] = \log|\mathcal{A}|^2 + i\Delta\varphi. \tag{9}$$

Hence, these two steps allow to extract $\Delta\varphi(X, Y)$ completely isolated from the background variation $\mathcal{A}(X, Y)$ and the reflectivity $\mathcal{B}(X, Y)$. Then the height distribution h and the associated positions $(y + \delta y)$ are calculated by means of the Eqs. (1) and (2).

3 Experimental setup

In this section, we describe both the experimental setup and the data processing technique employed in the experiments shown in Sect. 4. A discussion on the limitations of the method in terms of maximum range of measurement and resolution is presented as well.

3.1 Optical set-up

The complete experimental setup devised for our high-resolution surface deformation mapping technique is shown schematically in Fig. 2.

A Plexiglas channel with a test section of 1.5 m long, 0.5 m wide and 0.15 m high was built to hold the liquid whose free surface is to be studied.

In our experiments, water is employed as working liquid. In order to be able to project images onto the water surface the liquid's light diffusivity is enhanced by the addition of a white liquid dye (an standard, highly concentrated titanium dioxide pigment paste, commonly used for tinting water-based paints) which does not affect water's hydrodynamical properties. The optimum concentration level was established experimentally as a compromise between diluteness and high fringe contrast.
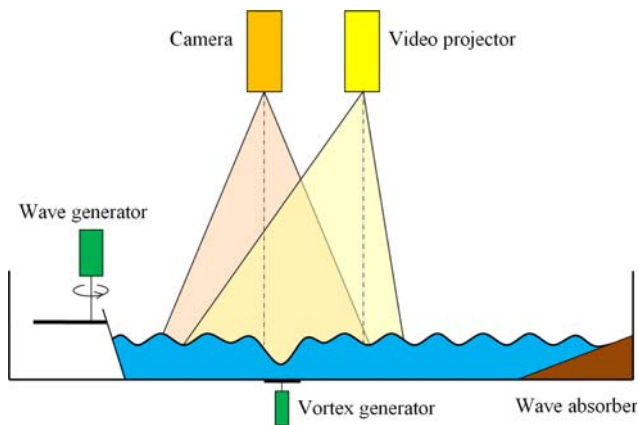
Fig. 2 Complete experimental setup

A concentration of 0.5% v/v, associated with a Michelson luminance contrast exceeding the threshold value of 0.85 was used in our experiments. It should be noted that this concentration value is well below the saturation point of 10% v/v, which assures that phase separation (either in the form of coexisting phases or suspension) cannot occur. Note that dye makes the liquid opaque, thus bulk measurements are possible using acoustical techniques (such as Ultrasonic Doppler Velocimetry) but not optical techniques (Particle Image Velocimetry, Laser Doppler Velocimetry).

Fringe pattern projection onto the free-surface is achieved by means of a computer-controlled digital videoprojector with a high resolution of 1,920 × 1,080 px², and 12-bit-depth per color. An important improvement arising from the use of a digital videoprojector is that we are able to project sinusoidal fringe patterns with a controlled wavelength (see Fig. 3). Usually, the projected

pattern is a square profile (Ronchi grating), extremely unadapted for Fourier analysis. Indeed, the use of a sinusoidal grating strongly increases the quality of the filtering process as well as the phase recovering. Another important improvement with a videoprojector compared to a slide-projector usually employed is that a videoprojector can project an image on a surface shifted with respect to its axis (see Fig. 2) and hence more centered to the camera axis. The videoprojector allows a correction of the projected image so that the image is not distorted and keeps the fringes' wavelength constant all over the image and maintains the original sharpness. However, due to the fact that the projected pattern varies discretely in space and is digitized in intensity, the video projector's resolution is lower than that of a slide projector.

For a given projection distance, the size of the projected optical field can be adjusted (by means of the projector zoom optics) to cover either a small or a relatively large area of the liquid's surface. In particular, we employed a projection distance of $L = 1$ m, which allowed us to work with projection windows of sizes ranging from approximately 36×20 to 80×45 cm² (covering roughly the channel's width).

The fringe patterns projected onto the liquid's free surface were recorded by a Fujifilm Finepix S2 Pro SRL-type digital still camera, with a 3,024 × 2,016 px² CCD and a color depth of 16-bits per color. In order to avoid any artifact from the camera's preprocessing algorithm (such as those coming from quantization, compression, color depth reduction, etc.) we worked with raw images which were later developed into portable pixmap (PPM) format at full color depth.
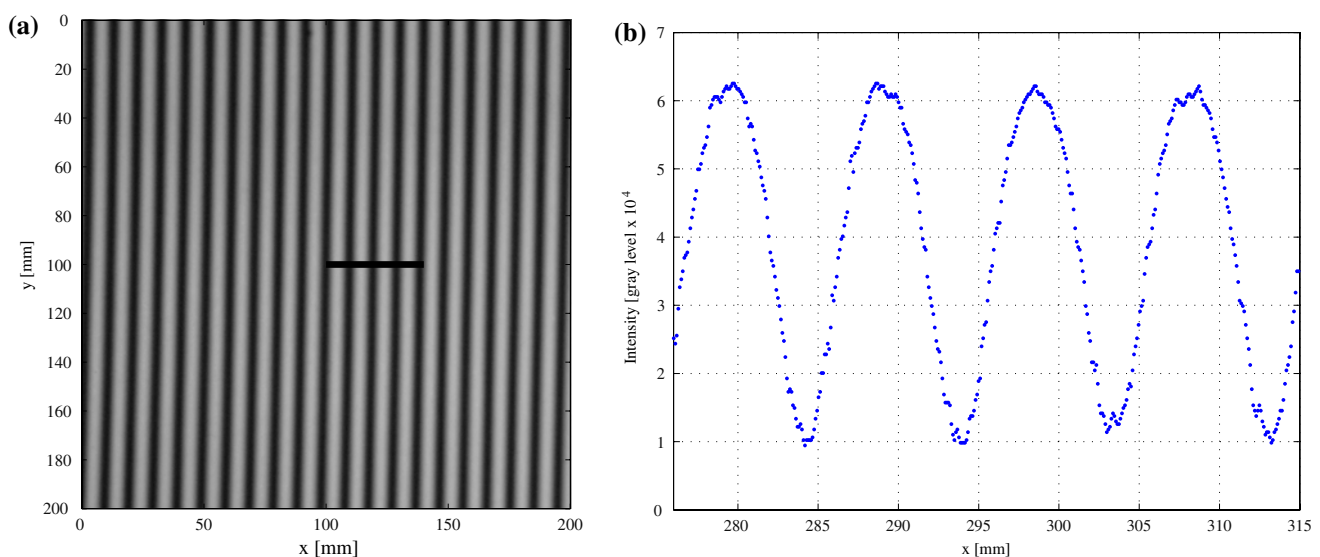

Fig. 3 a Sample image of the fringes projected onto an undeformed liquid surface as registered by the camera. **b** Intensity profile along the horizontal segment shown in *black* over the image *a*

The whole fringe projection and image capturing system is held over the channel supported by a mobile structure that allows for precise alignement and repositioning of the optical devices.

3.2 Wave and vortex generators

The channel is further equipped with two mechanisms to produce both global and localized controlled deformation of the liquid's surface (Fig. 2). On one end of the channel, a wave paddle system driven by a motor is employed to create plane sinusoidal surface waves with frequencies and amplitudes ranging from 1–500 Hz to 0.1 to 2 cm, respectively. At the opposite side of the channel, an inclined styrofoam beach of 1:3 slope acts as an absorber, avoiding unwanted surface wave reflections. Localized surface deformation is introduced in the form of a pinned vortex created by a 3 cm diameter rotating disk placed at the bottom of the basin, along the channel's longitudinal centerline. The disk, equipped with four plastic curved blades, is driven by a computer controlled servomotor in direction and speed up to 3,500 rpm.

An example of the free surface deformations that can be introduced by these two mechanisms is illustrated in Fig. 4. In the figure, plane surface waves coming from the left are deformed by the presence of the vortex (located in the center of each figure) and the occurrence of dislocations (Zhang et al. 1994; Vivanco and Melo 2004) on the wavefront is observed. In Sect. 4.2, a sample measurement of the FSD associated with this interaction obtained with the proposed technique is shown and discussed.

Fig. 4 FSD due to the interaction of the surface waves created by the paddle and the vortex generated by the rotating disk. This visualization has been created using grazing light in order to emphasize the texture of the surface. For reference, the field of view is approximately 50×30 cm^2 (Shutter speed 1/4,000 s)

3.3 Signal processing details

We describe in this section the signal processing details employed to accomplish the two steps described in the set of Eqs. (7–9). Step 1 is performed to eliminate the additive deviation $\mathcal{B}$ from I and I_0. Step 2 is then carried out in a procedure that slightly differs from the Hilbert transform described in Sect. 2.2, because the intensity of the projected fringes is not perfectly sinusoidal. Instead, a Fourier transform of $(I_0 - I_{\text{ref}})$ and $(I - I_{\text{ref}})$ is performed. Then each Fourier spectrum is filtered out to extract the ω_c neighbourhood of the frequency $2\pi/p_c$ which contains the height information. For the filtering, a gaussian window of adjustable size centered at that frequency is employed. The phases of the inverse Fourier transforms are then calculated to get $\varphi_0(Y)$ and $\varphi(Y)$. Finally, as the phases are determined modulo 2π, phase unwrapping is needed to obtain the continuous phase-shift over the image. For a comparison of several unwrapping algorithms applied to FTP, the reader is referred to Ghiglia and Pritt (1998) and to the recent reviews by Su and Chen (2004) and Zappa and Busca (2008) and references therein.

It is worth noting that, although FTP theory is based on continuous signals and a continuous Fourier transform, their experimental counterparts are inherently discrete. This induces an error in the recovered phase, particularly relevant for surface deformations of the highest spatial frequencies (e.g., high-frequency waves). However, Chen et al. (1999) have shown that this error can be minimized (as compared to the other experimental uncertainties) by an appropriate choice of the sampling frequency.

3.4 Error and limitations

In this section, we discuss (1) the error on the measured heights and (2) the maximum local slope measurable by this technique.

3.4.1 Uncertainties in the reconstructed height profiles

The relative error on the measured height can be written from Eq. (1)

$$\frac{\Delta h}{h} = \frac{\Delta(\Delta\varphi)}{\Delta\varphi} + \frac{\Delta L}{L} + \frac{\Delta D}{D} + \frac{\Delta p}{p}, \tag{10}$$

where we have used $\Delta\varphi \ll \pi D/p$. The uncertainty on h is therefore determined by the errors in the measured phase as well as those associated with the determination of the geometrical parameters (L, D, p) of the experimental setup. These two sources of uncertainty contribute differently to the final error on Δh, according to their nature. On the one hand, the contribution due to $\Delta\varphi$ is mainly associated with statistical fluctuations such as electronic noise and signal

processing (Fourier transform, filtering). Therefore, it produces a zero mean contribution whose standard deviation is responsible for an irreducible contribution to the uncertainty in h. On the other hand, the systematic errors associated with the determination of the geometrical parameters can be eliminated by calibrating the optical setup.

Calibration prior to laboratory testing can be carried out using any two points of known height. In our case, this was achieved by vertically displacing the reference (plane) surface by a fixed height, although it could also be done using a calibrated surface. Then, the geometrical parameters L and D are adjusted to obtain an optimum agreement between the original and the reconstructed profile.

Once calibrated, the system was tested in laboratory using a triangular prism of known characteristics. Figure 5 shows a superposition of several height profiles measured for the test object (corresponding to different positions on the perpendicular direction), as well as a zoomed view over a 1 mm region of those reconstructed profiles. In the figure, the profiles obtained with our measurement system are also compared to those given by a standard point laser displacement sensor (OptoNCDT 1401-50 by Micro-Epsilon), capable of measuring distances up to 50 mm with a (dynamic) resolution of 25 μm at a 1 kHz sampling rate. The residual fluctuations in this figure, with an amplitude of $\Delta h \sim 0.2$ mm, give the precision of our method, i.e., the minimum height difference the method is able to detect for this interrogation area. Note that the 0.2 mm corresponds as well to the size of the projected pixel and thus appears as a reasonable technical limitation.
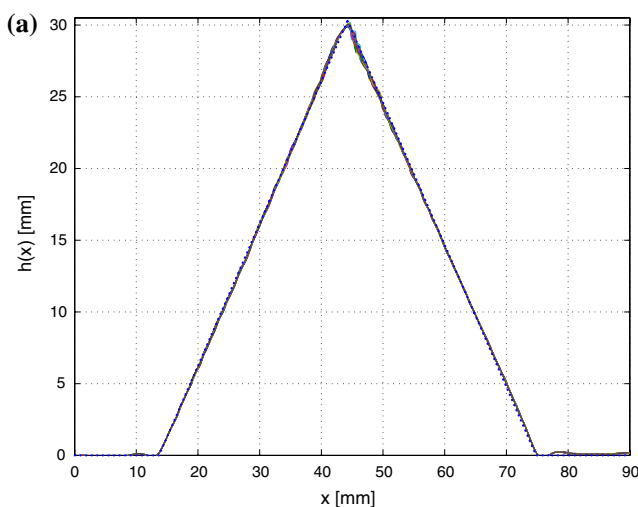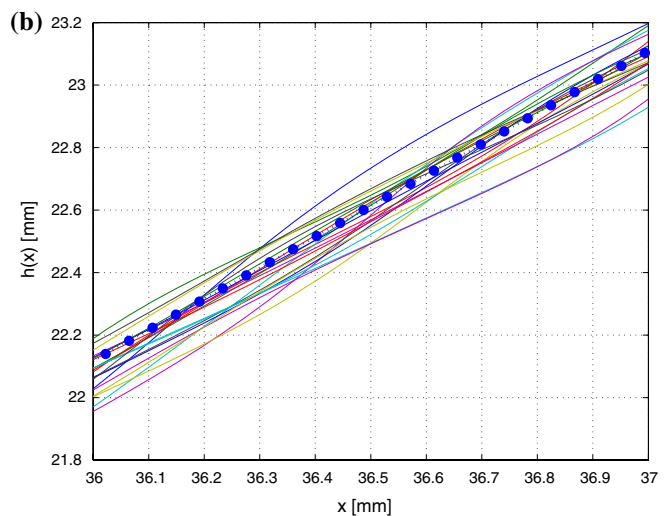
3.4.2 Typical length of variation of the measured height

There exists a limitation in the maximum slope this method is able to measure. This is because a sharper profile gives a larger Fourier spectrum (a limit being a delta function in the physical space that gives a constant Fourier transform). Thus, the error coming from the filtering increases when the slope of the profile increases. Although the filtering algorithm could be improved, a limitation exists given by the physical size of the projected pixels.

In order to estimate the error associated with the filtering process, we have conducted a numerical test on our data processing algorithm. For that, a gaussian-shaped height profile given by $h(y) = \exp\{y^2/s^2\}$ was chosen, which physically represents a localized deformation of width s on the surface under study. A projected fringe pattern of wavelength p was assumed and, using Eqs. (1–4), two synthetical images I_0 and I, corresponding respectively to the reference (plane) and deformed surfaces, were generated. It is worth noting that electronic noise present in the experiments was not considered in this study.

These two images were then processed by our algorithm (as described in Sect. 3.3), using a unitary gaussian filter of size σ_f centered at the projection (spatial) frequency $k_c = 2\pi/p_c$, ultimately leading to a reconstructed height profile h_r. Finally, the relative error in the reconstruction imposed by the filtering process, defined as $\varepsilon \equiv \sum |h_r - h| / \sum |h|$, was calculated. This process was then repeated for different widths of the filter window σ_f/k_c, and for varying s/p ratios.

Figure 6a illustrates the dependence of ε on the ratio s/p, for three particular values of σ_f/k_c, namely: 1/6, 1/3 and

Fig. 5 a Several height profiles measured for the triangular prism used for laboratory testing. **b** Zoom over a portion of the reconstructed profiles showing the precision of the method. In both cases, *dots* indicate the object's profile measured by a 25-μm resolution (point) laser displacement sensor, whereas continuous lines denote reconstructed profiles. Note that the weak fluctuations (of peak amplitude lower than 0.2 mm) observable at the flat regions next to the triangular profile are due to the abrupt change in slope, a feature which is not present in the case of most liquid surfaces
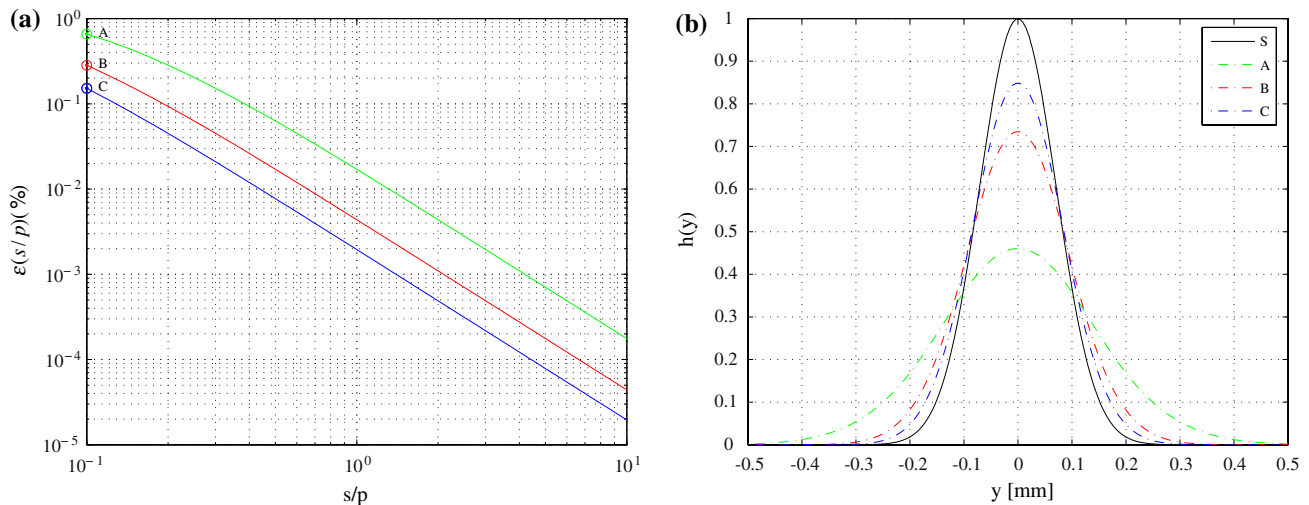
(a)

(b)

Fig. 6 Error associated to the data filtering and processing algorithm. **a** shows the error ε (as defined in the text) as a function of the dimensionless space variable defined as the ratio of the filter size to the period of the projected pattern. Each of the three curves shown corresponds to a particular value of the filter width (1/6, 1/3 and $1/2 \times 2\pi/p_c$ for the upper, middle and lower curves, respectively). **b** Shows three reconstructed profiles corresponding to the same value

$s/p = 10^{-1}$ over each curve in the **a**, compared to the original gaussian profile (shown in *black*). *Color* correspondence between curves in both panels has been conserved for reference purposes. Note that **b** shows a bad-case scenario to illustrate the influence of the filter width on the quality of the reconstruction; however, in practice, a set of parameters ensuring an error less than 10^{-4} % was used

1/2 (upper, middle and lower curves, respectively). This figure shows that the relative error effectively depends on the size of the filter window, assuming values lower than 10^{-2} for $s/p > 1$ and $\sigma_f/k_c > 1/6$ (typically, $1/3 \times 2\pi/p_c$ is used for the illustrative examples shown in Sect. 4). For a fixed value of the ratio $s/p = 0.1$, Fig. 6b shows three reconstructed profiles corresponding to points A, B and C in Fig. 6a, compared to the original gaussian-shaped profile S. Note that in this case, we have chosen a bad-case scenario (in which the characteristic width of the deformation is ten times smaller than the projected pattern's wavelength) in order to be able to show differences between the original and the reconstructed profiles. For $s/p \le 1$, however, these deviations from the original profile S are not discernible at the figure's resolution ($\varepsilon \le 10^{-2}\%$).

4 Some illustrative applications

In this section, the performance of the developed measuring system and analysis technique is illustrated with two experimental examples, showing its potential applicability to a vast variety of free-surface flows.

All the examples shown in this section have been measured using a projection distance $L = 1$ m, a projector–camera distance $D = 0.1$ m (thus, $L/D = 10$) and a fringe pattern of wavelength $p = 2$ mm. The shutter speed value employed in all cases is 1/4,000 s.

4.1 Spiral surface waves emitted by a vortex

The first example of application of this technique to free-surface flow measurements in our experimental set-up is devoted to the non-stationary emission of spiral surface waves from a vortex core. For a 3.5-cm depth liquid layer and a relatively high rotating speed (400 rpm) of the disk, a strong and fixed vertical vortex is created which, in addition, ocassionally emits weak amplitude spiral surface waves. These surface waves are barely noticeable to the naked eye. We present what is, to our knowledge, the first reported measurement of spiral waves emitted by a vortex available in the literature.

Figure 7 shows a sample free-surface reconstruction for the case of spiral waves emitted by a vortex obtained using the proposed technique. Note that this technique allows for the measurement of both the deep vortex core and the weak spiral waves over an interrogation area of size 30×45 cm^2. Although the wave amplitude is weak even near the source in comparison to the vortex core (25 mm in depth), the figure shows that the technique is able to detect and reconstruct remarkably well waves of amplitudes down to 0.2 mm. It is worth noting that this technique can discern perturbations of amplitudes throughout more than two orders of magnitude in a single shot measurement.

Qualitatively, similar spiral waves were theoretically predicted by Umeki and Lund (1997) in the shallow water regime and for penetrable boundary conditions at the vortex core. Moreover, Vivanco and Melo (2000) has

Fig. 7 Free surface deformations measured with the proposed technique, showing a set of spiral waves emitted by a vortex. Note the different height scales the method is able to discern: the vortex core is 25 mm in depth while the detectable amplitude for the spiral waves on the surface goes down to 0.2 mm. The overall interrogation area is 30×45 cm^2 in size
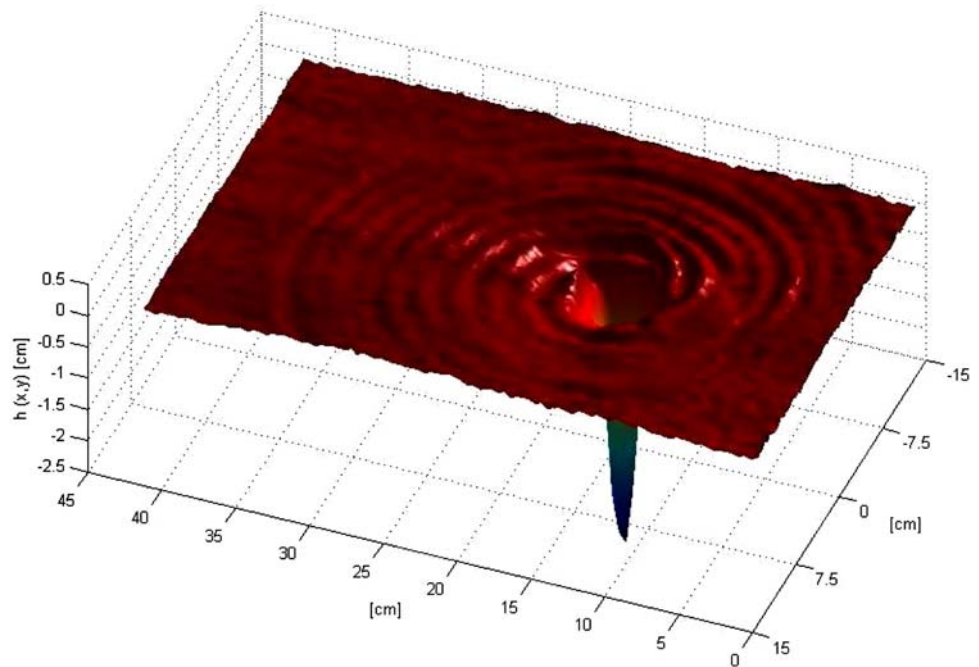
visualised spiral waves in an comparable experimental situation where they appear to be the natural solutions for a plane surface waves background flow in the presence of a vortex. An experimental study on these spiral waves is currently progress.

4.2 Vortex–surface–wave interaction

Free surface deformation due to water waves–vortex interaction is the subject of the second example of application shown in this section. The interest on the experimental study of such interactions is many fold. For instance, and from a fundamental point of view, Berry et al. (1980) have shown that wave–vortex interactions constitute an analogue in the frame of classical mechanics of the Aharonov–Bohm effect (Aharonov and Bohm 1959), in which the dynamics of a charged quantum particle is affected by the vector potential even in regions where the associated field vanishes. As opposed to the quantum case, the wavefront dislocations arising from the interaction are physically measurable. A detailed theoretical and numerical study of the scattering of dislocated wavefronts by vorticity structures and its relation with the Aharonov–Bohm effect was presented by Coste et al. (1999) and Coste and Lund (1999) for shallow water and dispersive waves, respectively.

Figure 8a shows a typical FSD field produced by the strong interaction between plane surface waves and a vortex as measured with the present technique. As in Fig. 4, incident waves propagate from left to right, impinging on the counterclockwise-rotating vortex and giving rise to strong deformations in the wavefronts. In this case, the depth of the liquid layer was set to 3 cm, and the disk rotates at 200 rpm. The associated vortex core is approximately 5 mm in depth, and the incident waves are characterized by a wavelength $\lambda \approx 6$ cm. The interrogation area over the surface is roughly 30×40 cm^2.

Both Fig. 8a and b show the same reconstructed FSD, only the range of the color palette is dilated in the latter to heights in the region [1.3] mm to emphasize the difference between hills and valleys, demonstrating the occurrence of dislocations in the wavefront.

A detailed study on the free surface deformations due to the interaction of water waves and a vertical vortex using this topographic technique is already underway and will be the subject of a following publication.

5 Concluding remarks

In order to accurately measure global time-evolving free-surface deformations we have adapted and strongly improved a measuring system and data processing technique based on FTP to the case of a liquid surface. The overall performance of the technique and the quality of the reconstruction have been greatly enhanced by the ability to project high-resolution sinusoidal fringe patterns (instead of using a Ronchi grating) controlled in wavelength. Careful reconstruction of the free-surface deformations was attained by considering the set of equations for h, δy and δx (corrections due to the last two equations being rarely taken into account in the literature).

Fig. 8 FSD measured for the
water wave–vortex interaction
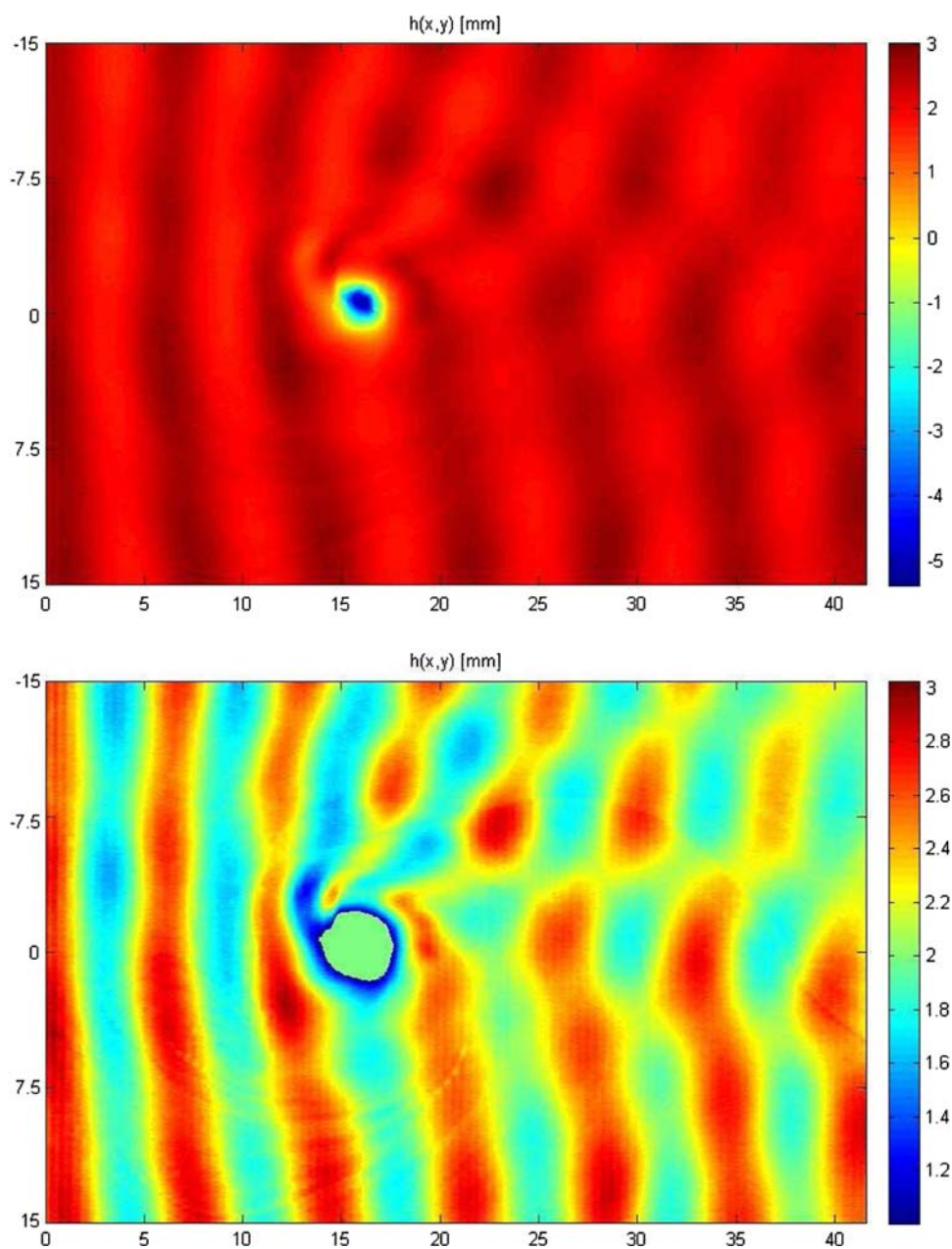
This experimental system is capable of measuring small perturbations over a large area; e.g., heights in the range from 0.2 to 100 mm, with a 0.2 mm vertical resolution over an interrogation window of 450×300 mm^2 sampled with an spatial resolution of 0.1 mm. As mentioned in Sect. 3.4, this absolute vertical resolution corresponds to the size of the projected pixel and thus depends, for a given projector's resolution, on the size of the sampled window over the surface under study.

It has the additional advantage of being easily scalable, so that it can be adapted for a specific application, ranging from small or medium scale laboratory experiments to large applications such as those considered in hydraulic engineering.

Finally, the application examples presented in this work demonstrate the large scope of applicability of this technique, which we believe constitutes a very useful and efficient tool to measure free-surface deformations on a vast variety of fluid dynamics' scenarios.

References

Aharonov Y, Bohm D (1959) Significance of electromagnetic potentials in the quantum theory. Phys Rev 115:485–491. doi: 10.1103/PhysRev.115.485

Benetazzo A (2006) Measurements of short water waves using stereo matched image sequences. Coast Eng 53:1013–1032

Berry MV, Chambers RG, Large MD, Upstill C, Walmsley JC (1980) Wavefront dislocations in the Aharonov–Bohm effect and its water wave analogue. Eur J Phys 1:154–162

Chan P-H, Bryanston-Cross PJ, Judge TR (1994) Studies of Fourier transform profilometry. In: Moorhead RJ, Silver DE, Uselton SP (eds) Proceedings of SPIE, visual data exploration and analysis, vol 2178, pp 165–176

Chen W, Hu Y, Su X, Tan S (1999) Error caused by sampling in Fourier transform profilometry. Opt Eng 38:1029–1034

Cochard S, Ancey C (2008) Tracking the free surface of time-dependent flows: image processing for the dam-break problem. Exp Fluids 44:59–71

Coste C, Lund F (1999) Scattering of dislocated wave fronts by vertical vorticity and the Aharonov–Bohm effect. II. Dispersive waves. Phys Rev E 60:4917–4925. doi:10.1103/PhysRevE.60.4917

Coste C, Lund F, Umeki M (1999) Scattering of dislocated wave fronts by vertical vorticity and the Aharonov–Bohm effect. I. Shallow water. Phys Rev E 60:4908–4916. doi:10.1103/PhysRevE.60.4908

Cox CS (1958) Measurement of slopes of high-frequency wind waves. J Mar Res 16(9):199–225

Dabiri D (2003) On the interaction of a vertical shear layer with a free surface. J Fluid Mech 480:217–232

Dabiri D, Gharib M (2001) Simultaneous free-surface deformation and near-surface velocity measurements. Exp Fluids 30:381–390

Gharib M (1994) Some aspects of near surface vortices. Appl Mech Rev 47:157–162

Gharib M, Weigand A (1996) Experimental studies of vortex disconnection and connection at a free surface. J Fluid Mech 321:59–86

Ghiglia DC, Pritt MD (1998) Two-dimensional phase unwrapping: theory, algorithms and software. Wiley, New York

Grant I, Stewart N, Padilla-Perez IA (1990) Topographical measurements of water waves using the projection moire method. Appl Opt 29:3981–3983

Maurel A, Cobelli P, Pagneux V, Petitjeans P (2009) Experimental and theoretical inspection of the phase-to-height relation in Fourier transform profilometry. Appl Opt 48(2):380–392. doi:10.1364/AO.48.000380

Moisy F, Rabaud M, Salsac K (2008) Measurement by digital image correlation of the topography of a liquid surface. Exp Fluids (submitted)

Patorski K (1993) Handbook of the Moire fringe technique. Elsevier, Amsterdam

Rajoub BA, Lalor MJ, Burton DR, Karout SA (2007) A new model for measuring object shape using non-collimated fringe-pattern projections. J Opt A Pure Appl Opt 9:66. doi:10.1088/1464-4258/9/6/S10

Ruban VP (2000) Interaction of a vortex ring with the free surface of an ideal fluid. Phys Rev E 62:4950–4958. doi:10.1103/PhysRevE.62.4950

Savelsberg R, van de Water W (2008) Turbulence of a free surface. Phys Rev Lett 100(3):034501. doi:10.1103/PhysRevLett.100.034501

Savelsberg R, Holten A, van de Water W (2006) Measurement of the gradient field of a turbulent free surface. Exp Fluids 41:629–640. doi:10.1007/s00348-006-0186-x

Su X, Chen W (2001) Fourier transform profilometry: a review. Opt Lasers Eng 35:263–284

Su X, Chen W (2004) Reliability-guided phase unwrapping algorithm: a review. Opt Lasers Eng 42:245–261

Takeda M, Mutoh K (1983) Fourier transform profilometry for the automatic measurement of 3-D object shapes. Appl Opt 22:3977–3982

Takeda M, Ina H, Kobayashi S (1982) Fourier-transform method of fringe-pattern analysis for computer-based topography and interferometry. J Opt Soc Am (1917–1983) 72:156

Tsubaki R, Fujita I (2005) Stereoscopic measurement of a fluctuating free surface with discontinuities. Meas Sci Technol 16:1894–1902. doi:10.1088/0957-0233/16/10/003

Umeki M, Lund F (1997) Spirals and dislocations in wave–vortex systems. Fluid Dyn Res 21:201–210

Vivanco F, Melo F (2000) Surface spiral waves in a filamentary vortex. Phys Rev Lett 85:2116–2119. doi:10.1103/PhysRevLett.85.2116

Vivanco F, Melo F (2004) Experimental study of surface waves scattering by a single vortex and a vortex dipole. Phys Rev E 69(2):026307. doi:10.1103/PhysRevE.69.026307

Walker DT, Chen C-Y, Willmarth WW (2006) Turbulent structure in free-surface jet flows. J Fluid Mech 91:223. doi:10.1017/S0022112095002680

Wright WB, Budakian R, Putterman SJ (1996) Diffusing light photography of fully developed isotropic ripple turbulence. Phys Rev Lett 76:4528–4531. doi:10.1103/PhysRevLett.76.4528

Wright WB, Budakian R, Pine DJ, Putterman SJ (1997) Imaging of Intermittency in ripple-wave turbulence. Science 278:1609

Zappa E, Busca G (2008) Comparison of eight unwrapping algorithms applied to Fourier-transform profilometry. Opt Lasers Eng 46:106–116

Zhang X (1996) An algorithm for calculating water surface elevations from surface gradient image data. Exp Fluids 21:43–48

Zhang X, Cox CS (1994) Measuring the two-dimensional structure of a wavy water surface optically: a surface gradient detector. Exp Fluids 17:225–237. doi:10.1007/BF00203041

Zhang Q-C, Su X-Y (2002) An optical measurement of vortex shape at a free surface. Opt Laser Technol 34:107–113

Zhang X, Dabiri D, Gharib M (1994) A novel technique for free-surface elevation mapping. Phys Fluids 6(9):S11–S11

Zhang X, Dabiri D, Gharib M (1996) Optical mapping of fluid density interfaces: concepts and implementations. Rev Sci Instrum 67:1858–1868